RESEARCH ARTICLES

BATTERIES

Halide segregation to boost all-solid-state lithium-chalcogen batteries

Jieun Lee[1]†‡, Shiyuan Zhou[1]†, Victoria C. Ferrari[1], Chen Zhao[1], Angela Sun[1], Sarah Nicholas[2], Yuzi Liu[3], Chengjun Sun[4], Dominik Wierzbicki[2], Dilworth Y. Parkinson[5], Jianming Bai[2], Wenqian Xu[4], Yonghua Du[2], Khalil Amine[1,6]*, Gui-Liang Xu[1,6]*

Mixing electroactive materials, solid-state electrolytes, and conductive carbon to fabricate composite electrodes is the most practiced but least understood process in all-solid-state batteries, which strongly dictates interfacial stability and charge transport. We report on universal halide segregation at interfaces across various halogen-containing solid-state electrolytes and a family of high-energy chalcogen cathodes enabled by mechanochemical reaction during ultrahigh-speed mixing. Bulk and interface characterizations by multimodal synchrotron x-ray probes and cryo–transmission electron microscopy show that the in situ segregated lithium halide interfacial layers substantially boost effective ion transport and suppress the volume change of bulk chalcogen cathodes. Various all-solid-state lithium-chalcogen cells demonstrate utilization close to 100% and extraordinary cycling stability at commercial-level areal capacities.

All-solid-state lithium-sulfur (Li-S) batteries (ASSLSBs) are highly desirable for electric vehicles because of their high theoretical energy density, safe operation, cost-effectiveness, and low supply chain risk (*1*). Despite the development of solid-state electrolytes (SSEs) with high room-temperature ionic conductivity (>10 mS cm^{-1}) (*2–4*), the cell performance of all-solid-state batteries still largely hinges on the charge transport and chemomechanical stability of the electrode-SSE interface (*5, 6*). Although the challenges of the Li-SSE interface are acknowledged, the poor electronic and ionic conductivity and large volume swelling (~80%) of sulfur result in severe intra- and interparticle reaction heterogeneity and chemomechanical failure of solid-solid interfaces after cycling (fig. S1) (*7, 8*).

Present efforts to improve the cell performance of ASSLSBs include nanostructured hosts (*9–11*), catalysts (*12*), additives (*13–15*), doping (*1, 16*), atomic layer deposition coating (*17*), and new SSEs (*18–20*). Although improvements have been achieved, these approaches still suffer from sluggish interfacial ion transport, resulting in low sulfur utilization (≤80%) and insufficient cycle life, particularly with increased areal sulfur loading (table S1). As a result, the projected cell energy densities of existing ASSLSBs remain low even when paired with thin SSEs (fig. S2). Moreover, elevated temperatures are often

needed to improve the reaction kinetics of thick electrodes (*1, 12, 13, 17, 19*), which would facilitate the formation of soluble polysulfides that has been deemed a critical barrier for long-life Li-S batteries (*21*) and would thus require specific cell design to prevent cross-talk (*1*). Last, these material innovations require multiple steps or long processing times to fabricate sulfur cathodes or composite electrodes (table S1), adding extra manufacturing cost.

It has been a common practice to mix electroactive materials, SSEs, and conductive carbon together to fabricate composite electrodes owing to the poor wetting ability of SSEs. This critical step dictates, to a great extent, the interfacial stability and charge transport of the composite electrodes but has long been deemed as a merely physical mixing process while underestimating the underlying interfacial chemistry. The existing efforts mostly focus on the physical properties of the composite electrodes, such as porosity, tortuosity, and the distribution of electrode components (*22, 23*). Leveraging chemical reactions between sulfur and SSEs represents an alternative strategy to forming an intimate interface through a wet mix process (*24*). However, owing to the insulating nature of sulfur, the ionic conductivity of the formed lithium polysulfidophosphate remains very low (*25*), leading to a low capacity retention of 63.9% after 250 cycles (*24*). In addition, this strategy relied on using sulfur-impregnated hosts and polar organic solvents that can potentially dissolve sulfide SSEs.

Having observed that nanocrystalline SSEs such as LiF could favor interfacial Li$^+$ transport despite the ionic insulating nature of the bulk phase (*13, 26, 27*), we considered whether nanosized lithium halides could segregate from bulk halogen–containing SSEs, such as argyrodites (*28*) and halides (*29*), and work as a plausible ion-transport booster. Inspired by the photoinduced phase segregation in mixed-halide perovskite solar cells (*30*), we observed a universal halide segregation at interfaces across a series of halogen-containing SSEs and a family of high-energy chalcogen (S, Se, SeS$_2$, Te) cathodes enabled by an ultrahigh mixing speed of 2000 rpm. The synergistic effects of heat striking and shear fracturing by the ultrahigh speed (UHS) mixing make it feasible to induce mechanochemical reaction to drive halide segregation from halogen-containing SSEs and the subsequent homogeneous deposition onto cathode particles during mixing (fig. S1). Such in situ segregated lithium halide interfacial layers boost the interfaces of various all-solid-state lithium-chalcogen cells, leading to exceptionally high utilization and long cycling stability (up to 450 cycles) at commercial-level areal capacities and room temperature (figs. S2 and S3). Moreover, no extra components (e.g., hosts, catalysts, dopants, etc.) and processing are required, contributing to substantial cost advantages compared with traditional material innovation approaches.

Mixing and structure analysis

We began our validation of the universal halogen-chalcogen chemistry for all-solid-state batteries by using a sulfur cathode and argyrodite Li$_6$PS$_5$Cl (LPSCl) SSE as an example. We prepared the optimal composite sulfur cathode by one-step UHS mixing of raw sulfur, LPSCl, and conductive carbon at 2000 rpm for 5 hours. Scanning electron microscopy (SEM) elemental mapping (fig. S4) showed an obvious separation of Cl and P (two signature elements of LPSCl) at the surface of LPSCl and a homogeneous distribution of Cl with S cathode particles after UHS mixing. By contrast, no Cl segregation was observed when lowering the mixing time to 1 hour (fig. S5) or reducing the mixing speed to 400 rpm (fig. S6).

A major challenge in using transmission electron microscopy (TEM) to achieve atomic-level insights into ASSLSBs lies in sulfur's vulnerability to local heat and high vacuum and the extreme sensitivity of LPSCl electrolyte to moisture and e-beam damage (*7, 31*). These limitations hinder high-resolution structural, chemical, and valence analysis at critical interfaces (*32, 33*), hampering the development of advanced solid-state batteries. To overcome this, aberration-corrected cryo-TEM and low-dose imaging were developed through extensive instrumental

[1]Chemical Sciences and Engineering Division, Argonne National Laboratory, Lemont, IL, USA. [2]National Synchrotron Light Source II, Brookhaven National Laboratory, Upton, NY, USA. [3]Center for Nanoscale Materials, Argonne National Laboratory, Lemont, IL, USA. [4]X-ray Science Division, Argonne National Laboratory, Lemont, IL, USA. [5]Advanced Light Source, Lawrence Berkeley National Laboratory, Berkeley, CA, USA. [6]Pritzker School of Molecular Engineering, The University of Chicago, Chicago, IL, USA. *Corresponding author. Email: amine@anl.gov (K.A.); xug@anl.gov (G.-L.X.) †These authors contributed equally to this work. ‡ Present address: Energy Storage Research Center, Korea Institute of Science and Technology (KIST), Seoul, Republic of Korea.

and experimental advancements (figs. S7 to S10), enabling direct observation of surface-to-bulk microstructural evolution in LPSCl and composite sulfur cathodes as well as their interface.

High-angle annular dark-field scanning transmission electron microscopy (HAADF-STEM) imaging and energy-dispersive x-ray spectroscopy (EDS) mappings revealed a uniform distribution of S, P, and Cl within the microsized LPSCl particle (Fig. 1A). Line scan analysis further confirmed an atomic ratio of 5:1:1 for S, P, and Cl, respectively (Fig. 1B). Quantitative analysis across surface and bulk regions (#1 to #3 in Fig. 1A) showed a Cl-to-P atomic ratio close to 1:1 (Fig. 1E), which was consistent with the bulk LPSCl structure. After UHS mixing, HAADF-STEM and EDS mapping revealed a clear Z-contrast variation and a Cl-rich segregation layer at the particle surface (Fig. 1C). The EDS line scan (Fig. 1D) confirmed a sharp increase in Cl concentration at the particle edges. Quantitative analysis in areas #4 to #6 of UHS-mixed LPSCl particles further showed a two to three times increase in the Cl-to-P ratio at the surface compared with the bulk (Fig. 1E). S-$L_{2,3}$ and Cl-$L_{2,3}$ edge electron energy loss spectroscopy (EELS) spectra at multiple regions further distinguished the distribution of sulfur and chlorine signals at the interface, which shows that the high-contrast regions (#8 to #10) are mainly composed of bulk LPSCl without Cl segregation, whereas the low-contrast regions (#7 and #11) consist of elemental sulfur and Cl-rich compounds (Fig. 1F and fig. S11).

The observed Cl segregation from LPSCl SSE is hypothesized to result from a mechanochemical reaction induced by UHS mixing (fig. S12). The frictional forces between particles generated localized heat sufficient to promote the Cl segregation, whereas shear forces contributed to particle size reduction and homogeneous mixing (34). As Li$^+$ is the only cation within the composite cathode and LiCl is a major electrochemical decomposition component of LPSCl (35, 36), we believe that the segregated Cl tends to exit as LiCl. In situ synchrotron x-ray diffraction (SXRD) during heating of a hand-mixed composite S/LPSCl/C mixture clearly evidenced the formation of LiCl (111) and (200) peaks as well as the reduction of LPSCl peaks with increased temperature (Fig. 1G and fig. S13). Similar results were observed during the heating of LPSCl and conductive carbon without sulfur, indicating that the LiCl segregation was not driven by the reaction with sulfur (fig. S14). EDS mapping (fig. S15) and quantification analysis results (Fig. 1E) of hand-mixed and heated composite S/LPSCl/C cathodes revealed similar Cl segregation, confirming the effect of the heating-striking force. In situ heating TEM experiments (figs. S16 and S17, and movies S1 and S2) further highlight the crucial role of the interplay between heating and shearing force during UHS mixing in addition to the microstructures of carbon additives (fig. S18) and electroactive materials (e.g., melting point) in promoting the halide segregation of halogen-containing solid electrolytes.

The microstructures of composite S cathodes prepared with different mixing times and speeds were unveiled by the SXRD (fig. S19A) and Rietveld refinement results (tables S2 to S5), x-ray pair distribution function analysis (fig. S19C), and Raman spectra (fig. S19D). No
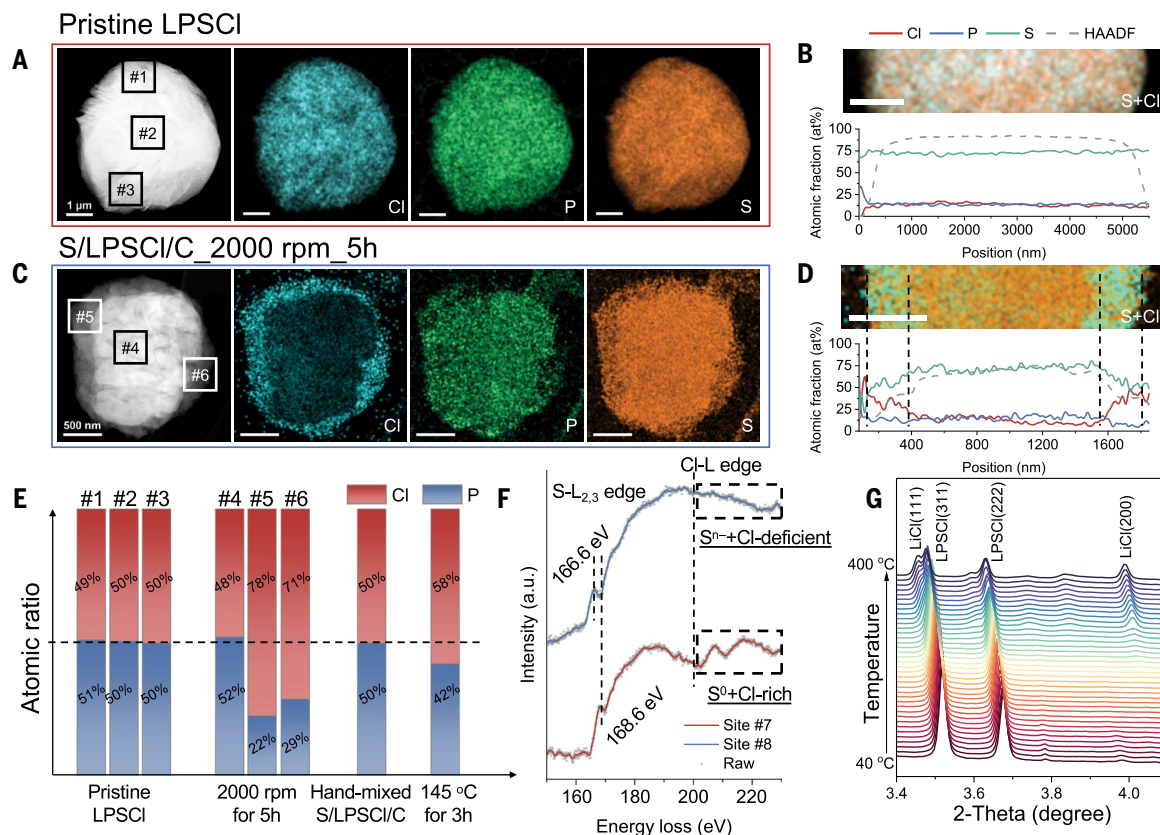
Fig. 1. Structure analysis of various composite S/LPSCl/C cathodes. (**A**) HAADF image with elemental mappings and (**B**) EDS line scan analysis of pristine LPSCl. (**C**) HAADF image with elemental mappings and (**D**) EDS line scan analysis of composite S/LPSCl/C cathode prepared with an ultrahigh mixing speed of 2000 rpm for 5 hours. The scale bars in (B) and (D) are the same as in (A) and (C), respectively. (**E**) Quantification of Cl-to-P atomic ratios for pristine Li$_6$PS$_5$Cl, composite S/LPSCl/C cathode with mixing at 2000 rpm for 5 hours, hand-mixed S/LPSCl/C cathode, and hand-mixed S/LPSCl/C cathode after heating at 145°C for 3 hours. (**F**) S-$L_{2,3}$ and Cl-$L_{2,3}$ edges EELS spectra of selected regions (fig. S11) in the composite S/LPSCl/C cathode with mixing at 2000 rpm for 5 hours. a.u., arbitrary units. (**G**) In situ SXRD patterns of the hand-mixed S/LPSCl/C cathode during heating from 40° to 400°C with a heating ramp rate of 10°C min^{-1}.

crystalline sulfur features were observed in all the composite S cathodes, indicating strong crystallinity loss of sulfur after mixing. By contrast, the 5-hour UHS-mixed sample showed pronounced reduction in both crystallite size and lattice parameter a of LPSCl (fig. S19B), presumably owing to the LiCl segregation. These findings were corroborated by x-ray photoelectron spectroscopy (XPS) characterization (figs. S20 to S22), reaffirming the formation of LiCl through partial segregation of LPSCl while ruling out the severe collapse of LPSCl to form Li_3P (37).

Universal halide segregation with chalcogen cathodes

We extended such a halide segregation strategy to a family of chalcogen cathodes and halogen-containing SSEs. Although cryo-TEM can preserve the native state of sulfur and its species, the real challenge lies in distinguishing critical interfaces due to the similar atomic numbers of sulfur and LPSCl anions. Introducing chalcogen cathodes such as Se and Te not only differentiates chalcogen signals from halogen-containing SSEs (Cl, Br, I) but also improves the understanding of cathode interfaces, as Se and Te exhibit greater stability than sulfur against e-beam damage and high vacuum. The UHS-mixed composite Se, SeS_2, and Te cathodes using LPSCl SSE demonstrated distinct Cl segregation from LPSCl and a strong overlap of Cl with Se or Te signals (figs. S23 and S24) regardless of the chalcogen type. Similarly, the composite S cathodes with various halogen-containing SSEs [Li_6PS_5Br (LPSBr), $Li_6PS_5Cl_{0.5}Br_{0.5}$ (LPSClBr), and $Li_6PSCl_{0.9}I_{0.1}$(LPSClI)] all

demonstrated halide segregation after UHS mixing (fig. S25). HAADF-STEM images and EDS mappings revealed halide segregation of both Cl and Br at the surface of Se in UHS-mixed composite Se/LPSCl/C (Fig. 2A) and Se/LPSBr/C cathodes (Fig. 2B). Quantitative analysis of multiple regions confirmed a substantial increase in the Cl-to-P and Br-to-P ratios, which rose by 1.5 to 4.6 times (Fig. 2C), similar to the Cl segregation observed in UHS-mixed composite S cathodes (Fig. 1). The composite Se cathodes did not form similar core-shell structures as the UHS-mixed composite S cathode owing to the difference in material properties between S and Se, such as melting point and ductility. Nevertheless, a uniform halide segregation (fig. S26) and carbon distribution (fig. S27) within the composite Se cathode was clearly evidenced by EDS mapping of multiple particles and regions.

To investigate the chemical state and spatial distribution of the segregated layer, we obtained EELS spectra and element mapping at specific sites in the annular dark-field STEM (ADF-STEM) image. Compared with the bulk LPSCl (i) and blank area (v), $Cl-L_{2,3}$ edge peaks located at 200 to 220 eV intensified at sites ii to iv (fig. S28), indicating Cl^- anion enrichment, based on standard KCl edge peaks. EELS mapping (Fig. 2D) further confirmed the formation of a LiCl-rich interfacial layer on the surfaces of Se particles after UHS mixing. Furthermore, Li-K (55 eV), $P-L_{2,3}$ (132 eV), $S-L_{2,3}$ (165 eV), and $Cl-L_{2,3}$ (200 eV) edge EELS characterization (Fig. 1E and fig. S29) revealed the formation of LiCl and Li- and Cl-deficient Li-P-S phase at the interface with a distinct Cl-to-P ratio. Interestingly, Cl-rich phases were consistently
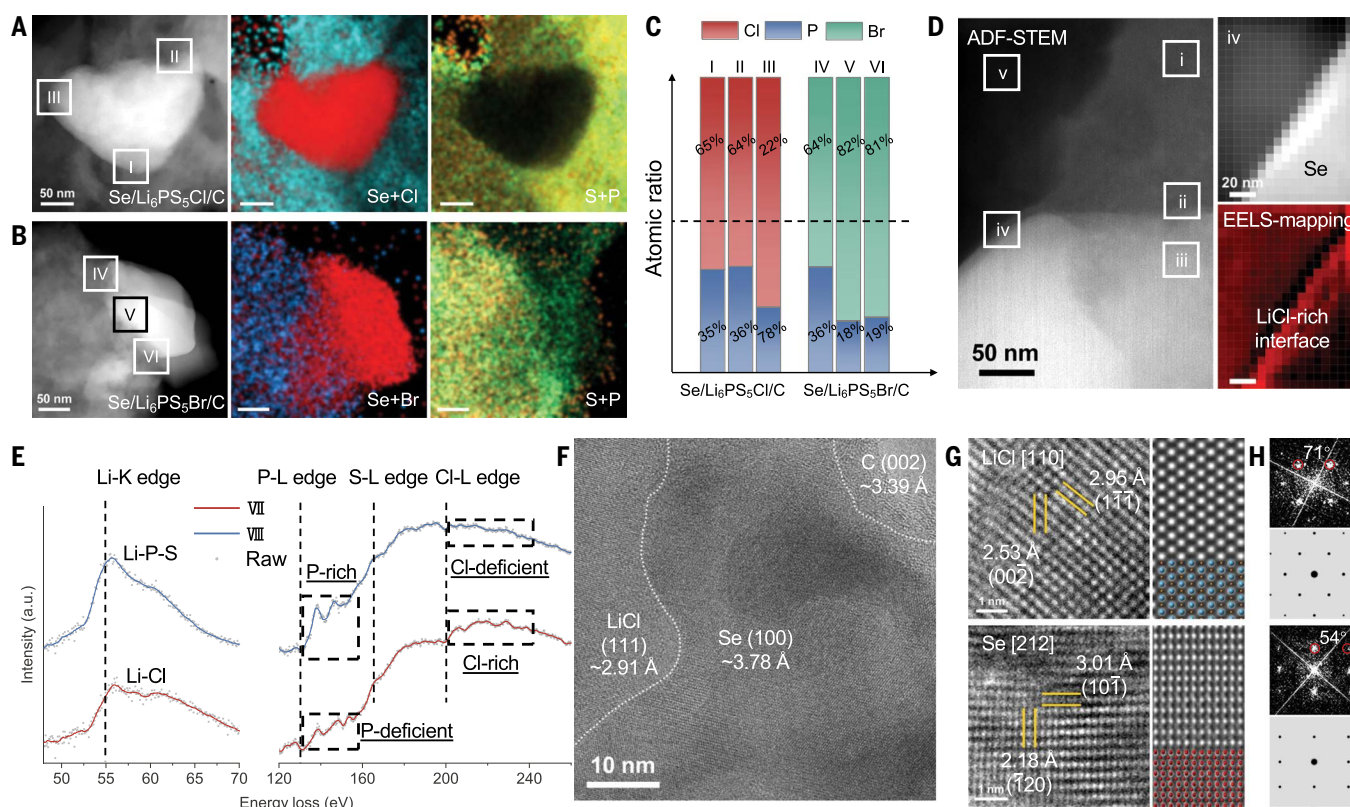
Fig. 2. Cryo-TEM validation of universal halide segregation. (**A**) HAADF image and the elemental mapping of composite Se/LPSCl/C cathode prepared with mixing at 2000 rpm for 5 hours. (**B**) HAADF image and the elemental mappings of composite Se/LPSBr/C cathode prepared with mixing at 2000 rpm for 5 hours. (**C**) Comparison of Cl-to-P and Br-to-P atomic ratios in the UHS-mixed composite Se cathodes, with data obtained from three different regions in each particle, as marked by the boxes in (A) and (B). (**D**) HAADF-STEM image (left), an enlarged view of the region marked as iv (top right), and EELS mapping of the same region (bottom right). (**E**) Li-K, $P-L_{2,3}$, $S-L_{2,3}$, and $Cl-L_{2,3}$ edges EELS spectra of selected regions (fig. S29) in the composite Se/LPSCl/C cathode with mixing at 2000 rpm for 5 hours. (**F**) HRTEM image showing Se covered by a layer of nanosized LiCl and carbon. (**G**) Acquired and simulated results of HRTEM images and (**H**) the corresponding FFT patterns and standard FFT patterns for cubic LiCl (top) and hexagonal Se (bottom) along the [110] and [212] directions, respectively. The Li, Cl, and Se atoms are represented by orange, blue, and red balls, respectively.

associated with P-deficient phases, whereas Cl-deficient phases corresponded to P-rich areas. High-resolution TEM (HRTEM) imaging of multiregions consistently revealed that nanocrystalline LiCl segregated alongside Se domains (Fig. 2F and figs. S30 and S31). A comparison of HRTEM images with simulated images (Fig. 2G), along with corresponding fast Fourier transform (FFT) patterns and standard FFT patterns (Fig. 2H), showed cubic Fm-3m LiCl with ($1\bar{1}\bar{1}$) and ($00\bar{2}$) crystal facets along the [110] zone axis and hexagonal P3121 Se with ($10\bar{1}$) and ($\bar{1}20$) surfaces along the [212] direction. These results provided solid evidence for the segregation of nanosized lithium halide from bulk halogen–containing SSEs and the subsequent deposition onto chalcogen cathode particles by UHS mixing.

Electrochemical performance

We examined the effect of halide segregation on the electrochemical performance of various chalcogen cathodes in all-solid-state cells with a Li-In anode, areal active material (e.g., S) loading of 4 mg cm^{-2}, and a stack pressure of ~70 MPa, unless specified otherwise. Moreover, we tested all the cells at room temperature (~25°C), lifting the limits of many reported ASSLSBs that relied on elevated working temperature (e.g., 60°C) to improve ion transport (table S1). Figure 3A shows the cycling performance of the UHS-mixed composite S cathodes with different processing times (1, 5, and 10 hours) at a current density of 0.67 mA cm^{-2}. Compared with the 1-hour and lower-speed (figs. S32 to S34) composite S cathodes without marked LiCl segregation, the 5-hour UHS-mixed composite S cathode delivered a high initial areal capacity of 6.28 mA·hour cm^{-2} and still retained 6.21 mA·hour cm^{-2} after 100 cycles, corresponding to a high capacity retention of 98.9%. Further increasing the mixing time to 10 hours still preserved the feature of LiCl segregation but resulted in a notable crystal structure collapse of LPSCl (fig. S35). As a result, both the 1- and 10-hour composite S cathodes exhibited rapid capacity decline during prolonged cycling. Whereas the ionic conductivity of bulk LPSCl SSEs decreased along with the time of UHS mixing, the Li$^+$ diffusion coefficient of the UHS-mixed composite cathodes increased substantially, with the 5-hour UHS-mixed composite S cathode demonstrating an increase 196 times greater than that of the 400-rpm cathode (fig. S36). These results highlight the crucial role of lithium halide segregation at the cathode-SSE interface in boosting the effective ion transport of the composite S cathodes, leading to exceptionally high sulfur utilization beyond many reported ASSBs under high S loading (fig. S3). Online cell stack pressure measurement during discharge and charge revealed a minimum pressure loss in the 5-hour UHS-mixed composite S cathode, indicating that the segregated LiCl layer could also suppress the volume change of sulfur particles during cycling (fig. S37). As a result, the voltage profiles during cycling of the 5-hour UHS-mixed composite S cathode showed a minimal polarization increase (Fig. 3B).

Long-term cycling performance of the 5-hour UHS-mixed composite S cathode was evaluated with an areal S loading of 2 mg cm^{-2} at 0.67 mA cm^{-2}. As shown, the all-solid-state cell could retain a reversible capacity of 3.00 mA·hour cm^{-2} after 450 cycles (Fig. 3C), leading to a high capacity retention of 93.2% after extended cycling. With an increased areal S loading of 4 mg cm^{-2} and a higher current density of 1.4 mA cm^{-2}, the all-solid-state cell could still deliver an initial discharge areal capacity of 6.35 mA·hour cm^{-2} (i.e., a high sulfur utilization of 95%) and a capacity retention of 80% after 450 cycles (Fig. 3D). The excellent cycling stability of the UHS-mixed composite S cathode was also demonstrated using Li metal as the anode (fig. S38). The 5-hour UHS-mixed composite S cathode still presented a high areal capacity and stable cycle life with a further increase of sulfur content to 32.5 wt % (fig. S39), leading to increased overall energy density. Evaluation under lower stack pressures of 36 and 18 MPa also demonstrated high capacity retention (fig. S40). These results corroborate
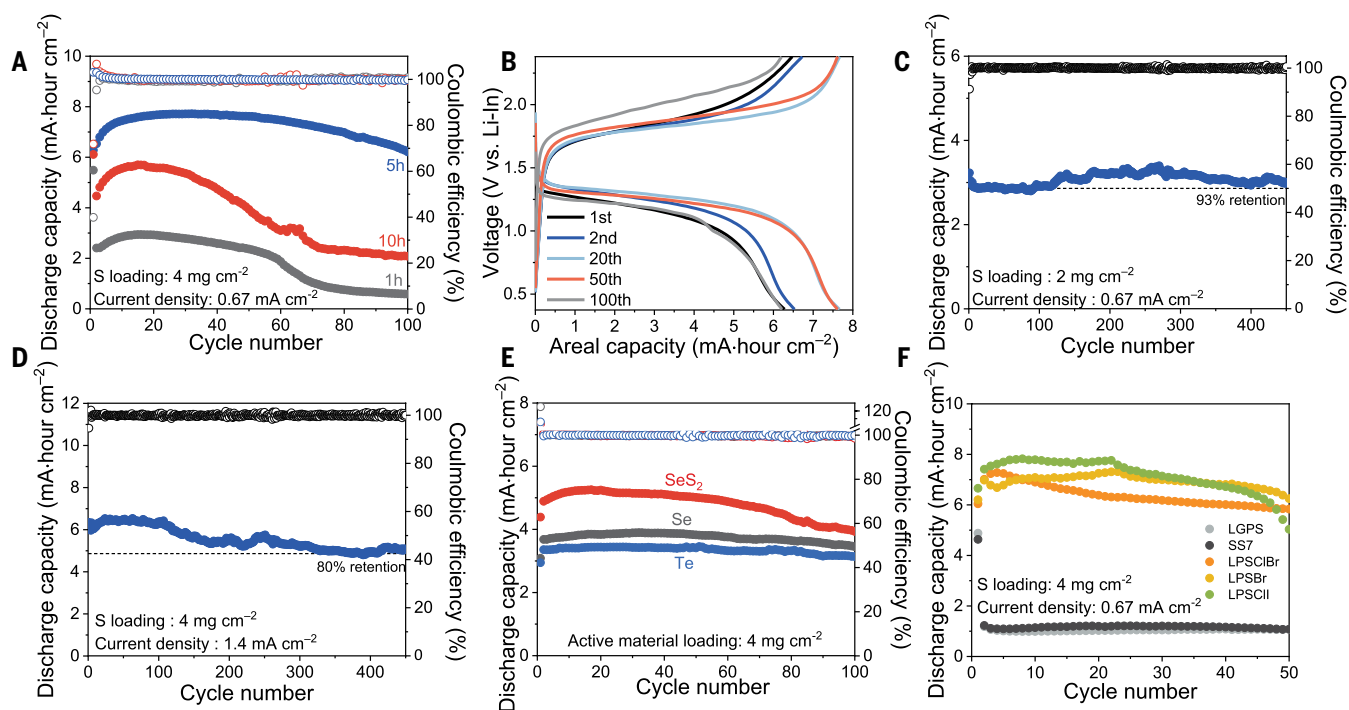

Fig. 3. Electrochemical performance of all-solid-state Li-chalcogen batteries. (**A**) Cycling performance of the UHS-mixed composite S/LPSCl/C cathodes with different times. (**B**) The corresponding discharge-charge curves of the 5-hour UHS-mixed composite S/LPSCl/C cathode. Long-term cycling performance of the 5-hour UHS-mixed composite S/LPSCl/C cathode with an areal S loading of (**C**) 2 mg cm^{-2} and (**D**) 4 mg cm^{-2} at room temperature. (**E**) Cycle performance of 5-hour UHS-mixed composite chalcogen cathodes at 0.27 (Se), 0.54 (SeS$_2$), and 0.56 (Te) mA cm^{-2} at room temperature. (**F**) Cycle performance of various 5-hour UHS-mixed composite S cathodes incorporating halogen-containing and halogen-free SSEs at room temperature.

the notable advantages of the present halide segregation strategy over many reported approaches in promoting the reaction kinetics and cycling stability of high-loading ASSLSBs (table S1 and figs. S2 and S3). Specifically, such in situ segregated nanosized lithium halide layers at the cathode-SSE interface produce results that differ greatly from those using bulk lithium halide additives, which suffer from intrinsic poor ion conductivity and low coverage (13–15).

The cycling performance of all-solid-state cells with various UHS-mixed composite chalcogen cathodes, including SeS$_2$, Se, and Te, are presented in Fig. 3E. As a result of the universal LiCl segregation, all these cells also demonstrated high utilization, stable cycling life, and good rate performance (fig. S41) at commercial-level areal capacities (3 to 5 mA·hour cm^{-2}) and room temperature. The broad effectiveness of halide segregation was further demonstrated through cycling tests of UHS-mixed composite S cathodes with various SSEs (Fig. 3F). Despite similar ionic conductivities among all the used SSEs (fig. S42), only cells incorporating halogen-containing SSEs (LPSBr, LPSClBr, and LPSClI) consistently exhibited high reversible capacity, whereas those with halogen-free SSEs (SS7 and Li$_{10}$GeP$_2$S$_{12}$) showed markedly lower capacity. Additionally, separate tests of hand-mixed composite S cathodes with and without heating treatment showed that the sulfur utilization was improved after heat treatment (fig. S43), which was well

aligned with heat-induced LiCl segregation as revealed by the cryo-TEM results (fig. S15).

In addition, it was noted that the UHS-mixed composite chalcogen cathodes exhibit greater capacity than their theoretical capacity limits (table S6), which can be attributed to the capacity contribution of the LPSCl SSE (36, 38). Although it has been shown that carbon would accelerate the decomposition of sulfide SSEs, particularly at high and low potential (39), the superior cycling stability of the 5-hour UHS-mixed composite chalcogen cathodes revealed that the interfacial halide segregation might help suppress these side reactions as well (figs. S44 to S46), adding extra capacity and energy density to the cell without sacrificing stability.

Postmortem characterization

We conducted multimodal synchrotron x-ray probes and cryo-TEM characterization of the cycled composite cathodes to elucidate the effect of halide segregation on the reaction pathways of all-solid-state lithium-chalcogen batteries. Figure 4A shows the S K-edge x-ray absorption near-edge structure (XANES) spectra of the 5-hour UHS-mixed composite S cathode at different discharge and charge states, along with the reference S, LPSCl, and Li$_2$S spectra. As shown, the pristine composite S cathode showed both features of S (2473 and 2480 eV)

and LPSCl (2472 eV). At half discharge or charge, no peaks at ~2470 eV were observed (13), indicating no formation of soluble polysulfides. After the first full discharge, the peak of LPSCl remained, but the peak of sulfur (2473 eV) shifted to higher energy (2474 eV), well aligned with the peak of reference Li$_2$S. After the first full charge, the peak of Li$_2$S disappeared along with the return of the S signal to its original position before discharge. Such high delithiation-lithiation reversibility enabled by LiCl segregation was still well maintained during extended cycling. The structural features of the 30th discharge composite S cathode well reassembled those of the first discharge feature. For comparison, the 10-hour UHS-mixed composite S cathode showed a notable residue of Li$_2$S features after the first charge, indicating decreased reaction reversibility (fig. S47).
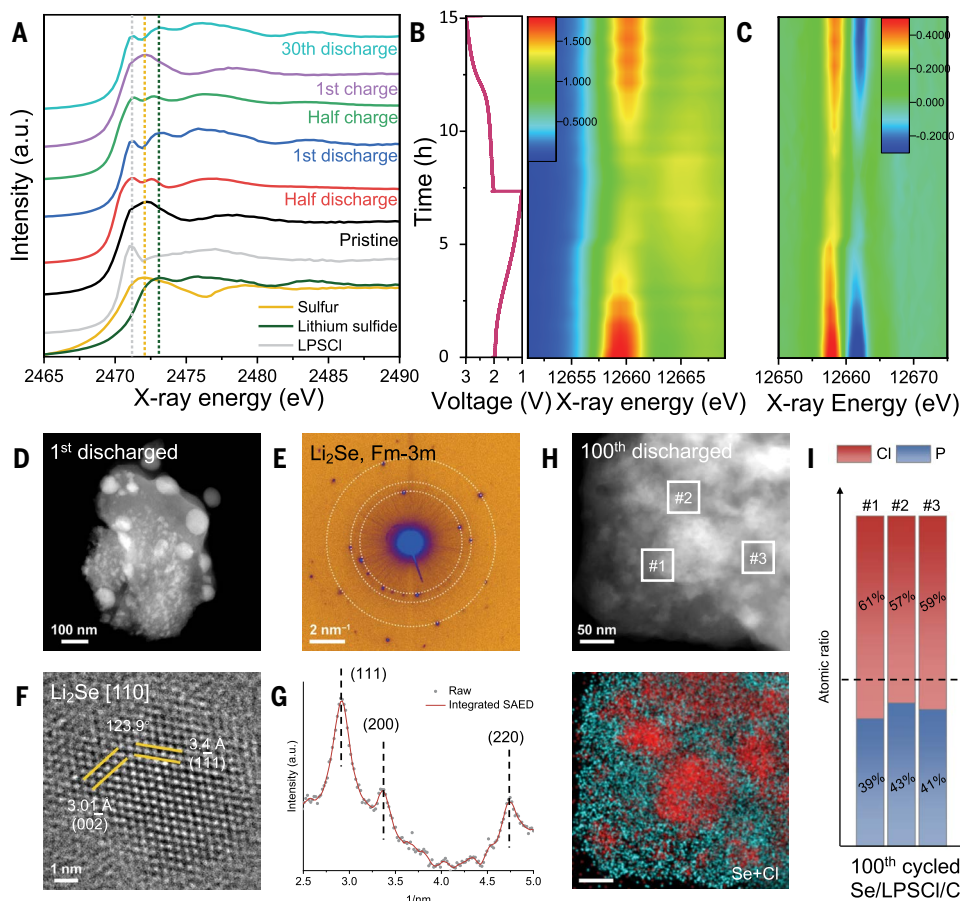
As both the sulfur cathode and LPSCl SSEs contain S signals, in situ Se K-edge XANES of the 5-hour UHS-mixed composite Se/LPSCl/C cathode was conducted to better probe whether any soluble long-chain polyselenides form during discharge and charge (Fig. 4B and fig. S48). As shown, the absorption edge position of Se did not undergo an obvious shift during the entire cycling process, whereas the absorption intensity gradually decreased during discharge and completely recovered at the end of charge, which was reaffirmed by the first derivatives of the Se K-edge XANES (Fig. 4C). These structural features are consistent with the reaction pathway of the Se cathode in polyselenide-free carbonate electrolytes (40) while being in sharp contrast with those involving conventional ether electrolytes with high polyselenide

Fig. 4. Postmortem analysis of UHS-mixed composite chalcogen cathodes. (A) S K-edge XANES spectra of the 5-hour UHS-mixed composite S/LPSCl/C cathode at different discharge and charge states. **(B)** Normalized two-dimensional contour plot of in situ Se K-edge XANES spectra of the 5-hour UHS-mixed composite Se/LPSCl/C cathode along with the discharge-charge profiles and **(C)** the corresponding derivative curve. **(D)** HAADF-STEM image, **(E)** SAED pattern, **(F)** HRTEM image, and **(G)** intensity integration profile from (E) of the 5-hour UHS-mixed composite Se/LPSCl/C cathode after the first discharge. **(H)** HAADF-STEM image and the elemental mappings of the 5-hour UHS-mixed composite Se/LPSCl/C cathode after 100 cycles. **(I)** Cl-to-P atomic ratios, with data from the three different regions in (H) marked by boxes.

solubility (*41*). In combination with S XANES, these results firmly reveal no formation of soluble intermediates in the LiCl-segregated composite chalcogen cathodes during discharge and charge, preserving the inherent nature of all-solid-state batteries that eliminate the use or formation of any liquid species. Comparison with composite Se cathodes prepared at different conditions further confirm the effect of halide segregation in promoting the reaction reversibility of composite cathodes (fig. S49).

The influences of LiCl segregation on the microstructures of discharge products and the consequent effects on the reaction kinetics and mechanical stability of composite chalcogen cathodes were further revealed. The in situ microcomputed tomography (μ-CT) of the 5-hour UHS-mixed composite S cathode during discharge and charge showed minimal electrode expansion and no formation of visible cracks or pores (fig. S50), confirming that the segregated LiCl interfacial layer could well suppress the volume change during cycling. Owing to the extreme sensitivity of sulfur and related species, such as Li_2S, we conducted HAADF-STEM on the 5-hour UHS-mixed composite Se/LPSCl/C cathode after the first discharge. As shown in Fig. 4D, a uniform distribution of nanoparticles (brighter contrast) embedded within the LPSCl matrix (darker contrast) was observed. The corresponding selected-area electron diffraction (SAED) pattern indicated a polycrystalline feature (Fig. 4E), with intensity integration peaks matching the (111), (200), and (220) planes of cubic Fm-3m Li_2Se (Fig. 4G). This suggests that these larger nanoparticles are aggregates of numerous smaller nanocrystalline particles. HRTEM imaging confirmed nanocrystalline Li_2Se oriented along the [110] direction, with particle sizes of about 10 nm (Fig. 4F). The formation of nanocrystalline discharge products not only reduces the energy barriers for nucleation and decomposition of Li_2Se, enabling more efficient reactions, but also mitigates the volume swelling and shrinkage during repeated cycling, ensuring long-term stability (*42*). Additionally, HAADF-STEM imaging and elemental mapping of the 5-hour UHS-mixed composite Se cathode after 100 cycles show that Cl segregation and deposition at the cathode surface remains well preserved (Fig. 4, H and I), with a Cl-to-P ratio close to that of the pristine state (Fig. 2C).

Overall, such universal halide segregation enabled by UHS mixing expands the scope of interface design to develop high-energy and long-life all-solid-state batteries. The in situ segregated nanosized lithium halide interfacial layer from a series of halogen-containing SSEs substantially boosts the interfaces for a family of chalcogen cathodes, even with commercially viable areal capacities and room temperature. The discovery of unexpected mixing-directed interfacial chemistries might inspire fundamental understandings and optimization of existing and emerging mixing technologies and pave the way to development and manufacturing of advanced ASSLSBs with future optimization of anode interface design and solid electrolyte engineering.

REFERENCES AND NOTES

1. J. Zhou et al., *Nature* **627**, 301–305 (2024).
2. Y. Li et al., *Science* **381**, 50–53 (2023).
3. Y. Zeng et al., *Science* **378**, 1320–1324 (2022).
4. R. Kato et al., *Nat. Energy* **1**, 16030 (2016).
5. S. Kalnaus, N. J. Dudney, A. S. Westover, E. Herbert, S. Hackney, *Science* **381**, eabg5998 (2023).
6. B. Zahiri et al., *Nat. Mater.* **20**, 1392–1400 (2021).
7. J. T. Kim et al., *Nat. Chem. Eng.* **1**, 400–410 (2024).
8. J. Lee et al., *Chem. Soc. Rev.* **53**, 5264–5290 (2024).
9. T. Jin et al., *Nano Lett.* **24**, 6625–6633 (2024).
10. X. Yao et al., *Adv. Energy Mater.* **7**, 1602923 (2017).
11. S. Xu et al., *Adv. Funct. Mater.* **31**, 2004239 (2021).
12. H. Zhong et al., *Adv. Energy Mater.* **13**, 2300767 (2023).
13. J. T. Kim et al., *Nat. Commun.* **14**, 6404 (2023).
14. H. Li et al., *Adv. Compos. Hybrid Mater.* **6**, 162 (2023).
15. M. Liu et al., *Nat. Commun.* **12**, 5943 (2021).
16. X. Li et al., *Adv. Mater.* **31**, 1808100 (2019).
17. H. Zhong et al., *Adv. Funct. Mater.* **34**, 2315925 (2024).
18. F. Pei et al., *Nat. Commun.* **15**, 351 (2024).
19. D. Wang et al., *Nat. Commun.* **14**, 1895 (2023).
20. S. Kim et al., *Nat. Commun.* **10**, 1081 (2019).
21. Q. Pang et al., *Nat. Energy* **3**, 783–791 (2018).
22. G. F. Dewald, S. Ohno, J. G. C. Hering, J. Janek, W. G. Zeier, *Batter. Supercaps* **4**, 183–194 (2021).
23. L. Fernandez-Diaz et al., *Chem. Eng. J.* **464**, 142469 (2023).
24. H. Kim, H.-N. Choi, J.-Y. Hwang, C. S. Yoon, Y.-K. Sun, *ACS Energy Lett.* **8**, 3971–3979 (2023).
25. Z. Lin, Z. Liu, W. Fu, N. J. Dudney, C. Liang, *Angew. Chem. Int. Ed.* **52**, 7460–7463 (2013).
26. Y. Liu et al., *Science* **375**, 739–745 (2022).
27. L. Hu et al., *ACS Nano* **18**, 8463–8474 (2024).
28. H.-J. Deiseroth et al., *Angew. Chem. Int. Ed.* **47**, 755–758 (2008).
29. X. Li et al., *Nat. Commun.* **15**, 53 (2024).
30. J.-P. Correa-Baena et al., *Science* **363**, 627–631 (2019).
31. Y. Nomura, K. Yamamoto, *Adv. Energy Mater.* **13**, 2203883 (2023).
32. J. E. Lee et al., *Adv. Mater.* **34**, e2200083 (2022).
33. Y. B. Song et al., *Nano Lett.* **20**, 4337–4345 (2020).
34. R. Schlem et al., *Adv. Energy Mater.* **11**, 2101022 (2021).
35. C. D. Alt et al., *Joule* **8**, 2755–2776 (2024).
36. D. H. S. Tan et al., *ACS Energy Lett.* **4**, 2418–2427 (2019).
37. J. Auvergniot et al., *Solid State Ion.* **300**, 78–85 (2017).
38. S. Wang et al., *Adv. Energy Mater.* **11**, 2101370 (2021).
39. S. Ohno, C. Rosenbach, G. F. Dewald, J. Janek, W. G. Zeier, *Adv. Funct. Mater.* **31**, 2010620 (2021).
40. Y. Cui, A. Abouimrane, C.-J. Sun, Y. Ren, K. Amine, *Chem. Commun.* **50**, 5576–5579 (2014).
41. Y. Cui et al., *J. Am. Chem. Soc.* **135**, 8047–8056 (2013).
42. S. Zhou et al., *Nature* **621**, 75–81 (2023).

SUPPLEMENTARY MATERIALS

science.org/doi/10.1126/science.adt1882
Materials and Methods; Figs. S1 to S50; Tables S1 to S6; References (*43–68*); Movies S1 and S2

Submitted 16 September 2024; accepted 25 March 2025
10.1126/science.adt1882